Phase Transitions of Adsorbed Atoms on the Surface of a Carbon Nanotube

Zenghui Wang, *et al.*

Science **327**, 552 (2010);
DOI: 10.1126/science.1182507

(*10*), Wnt (*11*), and laminin (*6*, *7*), could modulate the cAMP or cGMP level in neurons (*12*, *38*–*43*). Localized exposure to one or more of such factors may create a cytoplasmic asymmetry for axon/dendrite initiation. Perturbation of the cAMP/cGMP level resulted in neuronal polarization defects in the developing cortex (figs. S4 and S5), but the cAMP/cGMP-modulating extracellular factors that are responsible for polarizing the neurons in vivo remain to be identified. In a model for distinct actions of local versus global cAMP/cGMP signaling (fig. S7), we propose that axons and dendrites are induced via localized cAMP and cGMP signals, and local antagonistic interactions between cAMP and cGMP pathways ensure that axon initiation is accompanied by the inhibition of dendrite formation, and vice versa. The cAMP signal acts through phosphorylated LKB1 (*12*) and GSK-3β (*8*, *16*) and their downstream effectors, which may converge with the PI3K pathway at several levels to promote axon initiation (*15*, *19*, *44*–*46*), whereas the cGMP signal suppresses axon formation via reciprocal down-regulation of cAMP/PKA-dependent phosphorylation of LKB1 and GSK-3β (Fig. 3), as well as specifically promotes dendrite growth (Fig. 5) via cellular processes yet to be identified (fig. S7).

Long-range inhibitory signaling in neurons has been reported. Local contact of a neurite with a target cell (*47*) or laminin-coated surface (*6*, *7*), or local perfusion of a neurite with forskolin (*48*), all led to growth inhibition of distant neurites. This inhibitory effect may be caused by the long-range self-suppression of cAMP, although the mechanism underlying this long-range cAMP self-antagonism remains to be elucidated. The absence of long-range signaling resulting from local cGMP elevation suggests the framework of axon dominance signaling in the coordinated axon/dendrite differentiation; whereas local cAMP/cGMP reciprocal regulation helps to channel the differentiation process along either an axonal or dendritic route, the long-range cAMP self-suppression ensures the formation of only one axon.

References and Notes

1. N. Arimura, K. Kaibuchi, *Nat. Rev. Neurosci.* **8**, 194 (2007).
2. A. P. Barnes, D. Solecki, F. Polleux, *Curr. Opin. Neurobiol.* **18**, 44 (2008).
3. F. C. de Anda *et al.*, *Nature* **436**, 704 (2005).
4. K. Goslin, G. Banker, *J. Cell Biol.* **108**, 1507 (1989).
5. C. Jacobson, B. Schnapp, G. A. Banker, *Neuron* **49**, 797 (2006).
6. T. Esch, V. Lemmon, G. Banker, *J. Neurosci.* **19**, 6417 (1999).
7. C. Ménager, N. Arimura, Y. Fukata, K. Kaibuchi, *J. Neurochem.* **89**, 109 (2004).
8. T. Yoshimura *et al.*, *Cell* **120**, 137 (2005).
9. J. S. Da Silva, T. Hasegawa, T. Miyagi, C. G. Dotti, J. Abad-Rodriguez, *Nat. Neurosci.* **8**, 606 (2005).
10. C. E. Adler, R. D. Fetter, C. I. Bargmann, *Nat. Neurosci.* **9**, 511 (2006).
11. M. A. Hilliard, C. I. Bargmann, *Dev. Cell* **10**, 379 (2006).
12. M. Shelly, L. Cancedda, S. Heilshorn, G. Sumbre, M. M. Poo, *Cell* **129**, 565 (2007).
13. M. Fivaz, S. Bandara, T. Inoue, T. Meyer, *Curr. Biol.* **18**, 44 (2008).
14. M. Toriyama *et al.*, *J. Cell Biol.* **175**, 147 (2006).
15. S. H. Shi, L. Y. Jan, Y. N. Jan, *Cell* **112**, 63 (2003).
16. H. Jiang, W. Guo, X. Liang, Y. Rao, *Cell* **120**, 123 (2005).
17. J. C. Schwamborn, A. W. Püschel, *Nat. Neurosci.* **7**, 923 (2004).
18. M. Kishi, Y. A. Pan, J. G. Crump, J. R. Sanes, *Science* **307**, 929 (2005).
19. A. P. Barnes *et al.*, *Cell* **129**, 549 (2007).
20. C. G. Dotti, C. A. Sullivan, G. A. Banker, *J. Neurosci.* **8**, 1454 (1988).
21. A. M. Craig, G. Banker, *Annu. Rev. Neurosci.* **17**, 267 (1994).
22. A. M. Lohof, M. Quillan, Y. Dan, M. M. Poo, *J. Neurosci.* **12**, 1253 (1992).
23. M. Nishiyama *et al.*, *Nature* **423**, 990 (2003).
24. N. Buttner, S. A. Siegelbaum, *J. Neurophysiol.* **90**, 586 (2003).
25. H. C. Hartzell, R. Fischmeister, *Nature* **323**, 273 (1986).
26. A. Hempel, T. Noll, A. Muhs, H. M. Piper, *Am. J. Physiol.* **270**, H1264 (1996).
27. C. Peña-Rasgado, V. A. Kimler, K. D. McGruder, J. Tie, H. Rasgado-Flores, *Am. J. Physiol.* **267**, C1319 (1994).
28. N. D. Goldberg *et al.*, *Adv. Cyclic Nucleotide Res.* **5**, 307 (1975).
29. M. Zaccolo, M. A. Movsesian, *Circ. Res.* **100**, 1569 (2007).
30. L. M. DiPilato, X. Cheng, J. Zhang, *Proc. Natl. Acad. Sci. U.S.A.* **101**, 16513 (2004).
31. V. O. Nikolaev, S. Gambaryan, M. J. Lohse, *Nat. Methods* **3**, 23 (2006).
32. J. Zhang, Y. Ma, S. S. Taylor, R. Y. Tsien, *Proc. Natl. Acad. Sci. U.S.A.* **98**, 14997 (2001).
33. F. S. Menniti, W. S. Faraci, C. J. Schmidt, *Nat. Rev. Drug Discov.* **5**, 660 (2006).
34. T. Saito, N. Nakatsuji, *Dev. Biol.* **240**, 237 (2001).
35. F. Bradke, C. G. Dotti, *Science* **283**, 1931 (1999).
36. H. Witte, D. Neukirchen, F. Bradke, *J. Cell Biol.* **180**, 619 (2008).
37. H. Witte, F. Bradke, *Curr. Opin. Neurobiol.* **18**, 479 (2008).
38. F. Polleux, T. Morrow, A. Ghosh, *Nature* **404**, 567 (2000).
39. H. J. Song, G. L. Ming, M. M. Poo, *Nature* **388**, 275 (1997).
40. G. L. Ming *et al.*, *Neuron* **19**, 1225 (1997).
41. Y. Gao, E. Nikulina, W. Mellado, M. T. Filbin, *J. Neurosci.* **23**, 11770 (2003).
42. K. Togashi *et al.*, *Neuron* **58**, 694 (2008).
43. V. H. Höpker, D. Shewan, M. Tessier-Lavigne, M. M. Poo, C. Holt, *Nature* **401**, 69 (1999).
44. O. Ossipova, N. Bardeesy, R. A. DePinho, J. B. A. Green, *Nat. Cell Biol.* **5**, 889 (2003).
45. Y. J. Choi *et al.*, *Genes Dev.* **22**, 2485 (2008).
46. J. Wildonger, L. Y. Jan, Y. N. Jan, *Genes Dev.* **22**, 2447 (2008).
47. D. J. Goldberg, S. Schacher, *Dev. Biol.* **124**, 35 (1987).
48. J. Q. Zheng, Z. Zheng, M. M. Poo, *J. Cell Biol.* **127**, 1693 (1994).

49. We thank R. Thakar, S. Li, M. Nasir, and D. Liepmann (University of California at Berkeley) for help with poly(dimethylsiloxane) microfluidic molds; J. Zhang (Johns Hopkins University) for the ICUE and AKAR FRET probes; M. J. Lohse (University of Wurzburg) for the cGES-DE5 FRET probe; M. Feller and S. Pautot (University of California at Berkeley) for advice on FRET imaging and bead coating; and M. Hung for help with culture preparations. This work was supported in part by a grant from the National Institutes of Health (NS-22764).

Supporting Online Material

www.sciencemag.org/cgi/content/full/327/5965/547/DC1
Materials and Methods
SOM Text
Figs. S1 to S7

27 July 2009; accepted 10 December 2009
10.1126/science.1179735

REPORTS

Phase Transitions of Adsorbed Atoms on the Surface of a Carbon Nanotube

Zenghui Wang, Jiang Wei, Peter Morse, J. Gregory Dash, Oscar E. Vilches, David H. Cobden*

Phase transitions of adsorbed atoms and molecules on two-dimensional substrates are well explored, but similar transitions in the one-dimensional limit have been more difficult to study experimentally. Suspended carbon nanotubes can act as nanoscale resonators with remarkable electromechanical properties and the ability to detect adsorption at the level of single atoms. We used single-walled carbon nanotube resonators to study the phase behavior of adsorbed argon and krypton atoms as well as their coupling to the substrate electrons. By monitoring the resonance frequency in the presence of gases, we observed the formation of monolayers on the cylindrical surface, phase transitions within them, and simultaneous modification of the electrical conductance.

Films of atoms or molecules adsorbed on surfaces exhibit many kinds of ordering that reflect interactions between the adsorbates as well as with the surface. One of the simplest model systems, rare gases on bulk exfoliated graphite, exhibits a huge range of two-dimensional (2D) phenomena within the first adsorbed layer, including 2D melting, transitions between solids that are either commensurate or incommensurate with the graphene lattice, and critical behavior (*1*, *2*). Here, we explore the phase behavior of argon and krypton on carbon nanotubes, where the dimensionality of the substrate approaches the 1D limit, and report effects on the electronic conductance that reflect adsorbate-substrate interactions. We map out this phase behavior using nanomechanical resonators based on individual suspended single-walled nanotubes (SWNTs) (*3*–*6*). This platform combines remarkable electrical (*7*–*9*) and electromechanical (*10*–*12*) properties with extreme mass sensitivity (*13*–*15*) and allows simultaneous measurement of both the precise amount of adsorbed substance and its effect on the electrical

Department of Physics, University of Washington, Seattle, WA 98195–1560, USA.

*To whom correspondence should be addressed. E-mail: cobden@u.washington.edu

properties. Our approach avoids problems of heterogeneity that have complicated previous explorations of this regime based on conventional techniques that require the use of bulk nanotube samples (*16*–*18*).

Suspended nanotube devices were made by prefabricating the electrodes and trench, and then growing the SWNTs in the last step (*19*) to avoid any chemical exposure that might contaminate the pristine nanotube surface (Fig. 1A). Mechanical resonances appear as sharp features in the current signal during frequency sweeps (*20*). The frequency f_{res} of each resonance decreases with increasing pressure P as gas adsorbs (*20*), as illustrated in Fig. 1B for Kr at 77 K. Equilibrium is established in seconds after a small pressure change (Fig. 1C), and f_{res} is a reproducible function of P (Fig. 1D).

We deduce the adsorbed mass by assuming that at a given temperature f_{res} varies as $\rho^{-1/2}$, where the total mass per unit length ρ is the sum of that of the bare nanotube, ρ_0, and of the adsorbates, $\Delta\rho$. (This assumption will be justified below.) The fractional mass increase of the nanobalance is then $\Delta\rho/\rho_0 = (f_0/f_{res})^2 - 1$, where $f_0 = \lim_{P \to 0} f_{res}$. Because f_0 is determined separately at each temperature T, any variation of the resonance frequency with T, such as might result from thermal expansion, is factored out. If m_C and m_{ads} are the atomic masses of carbon and the adsorbed species respectively, then the quantity

$$\varphi = (\Delta\rho/m_{ads})/(\rho_0/m_C) = m_C/m_{ads}\,[(f_0/f_{res})^2 - 1] \quad (1)$$

is the number of adsorbed atoms per carbon atom; Fig. 1E shows an example of an isotherm of φ versus P derived in this way.

The assumed $\rho^{-1/2}$ scaling of f_{res} requires that the change in elastic properties is negligible compared with the fractional change in mass. This assumption can be made because the covalent C–C bond is two orders of magnitude stronger than the van der Waals attraction between adsorbates. We also must assume that the mass is distributed uniformly over the nanotube surface, which would not be the case if part of the surface were contaminated, or if a denser phase appeared preferentially at the ends or in the middle in response to long-range forces. Nonuniformity would cause different vibrational modes to shift in different ways. However, we have found that f_0/f_{res} does not depend on which mode is used and also that it is insensitive to substrate gate voltage V_g, up to about 8 V (see, for example, Fig. 1E). Taken together with the results described below, these observations indicate that many of our devices consist of single-walled nanotubes in which φ is a good measure of the coverage (number of adsorbates per surface atom) and that the coverage is uniform.

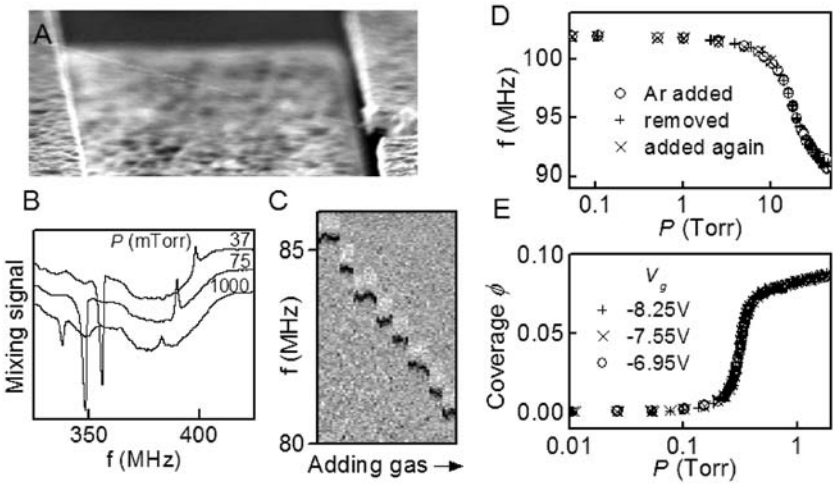

Fig. 1. Detecting adsorption on a single vibrating nanotube. (**A**) Electron micrograph of a nanotube spanning a 2-μm wide trench between Pt contacts. (**B**) Line traces of the mixing current signal showing resonances shifting with Kr gas pressure for device YB3 (0.5-μm gap) at 77.4 K and V_g = 9.58 V. (**C**) Grayscale of the mixing current signal for a series of frequency sweeps taken during a sequence of Kr pressure increments, one roughly every 3 min, demonstrating rapid equilibration, for device YB1 (2-μm gap) at 77.4 K. (**D**) Variation of resonance frequency with Ar pressure for YB1, showing high reproducibility. (**E**) Variation of coverage parameter φ obtained using Eq. 1 with Kr pressure for YB1, demonstrating little sensitivity to gate voltage.

Isotherms of φ versus P for Ar are dominated by a large, smooth step, as shown in Fig. 2 for device YB3. A similar step is well known in conventional volumetric isotherms on bulk exfoliated graphite and is characteristic of the densification of a supercritical 2D fluid (F), which occurs above 56 K, the 2D liquid (L)–vapor (V) critical point of Ar on graphite (*2*, *21*, *22*). The colder Ar isotherms also show a second, smaller step at $\varphi \approx 0.24$ (see the inset of Fig. 2). A similar second step is seen for Ar on graphite (*22*) when the fluid freezes to a 2D incommensurate solid (IS). Accordingly, we anticipate an L+V coexistence region at lower temperatures as indicated by the dotted line, and we expect the F+IS coexistence region to have the form indicated by the dashed lines. We note that corresponding features occur at higher pressures on nanotubes than on graphite, reflecting the expected weaker binding of atoms to a nanotube surface than to bulk graphite (*23*).

We now discuss how this phase behavior changes for Kr, which is larger and more polarizable than Ar. Isotherms of Kr on device YB3 exhibit a dramatic vertical step followed by two smaller steps (Fig. 3). Again, these resemble conventional volumetric isotherms of the same substance on exfoliated graphite (*24*) but shifted to higher pressures. The size and sharpness of the large step implies not only a first-order phase transition but also excellent substrate homogeneity, consistent with the absence of grain boundaries or imperfections on the surface of this SWNT. The first plateau, between the first two steps, is narrow and easily missed; it is resolved in the 77.4 K data here but not the 73.7 K data.

Whereas Ar does not form any commensurate phase on graphite, Kr condenses from a low-density 2D vapor (V) to a commensurate solid (CS) with one Kr atom per six C atoms (*25*), as indicated in the left inset to Fig. 3. At higher pressure, it converts to an IS (*26*). The first plateau in our Kr isotherms, whenever resolved, is centered at φ =1/6, corresponding to the coverage of the commensurate solid and implying that the first step is a V-CS transition. The highest plateau reached is likely to be the IS, whereas the intermediate plateau is of unknown nature but may be related to a proposed reentrant fluid phase (*27*).

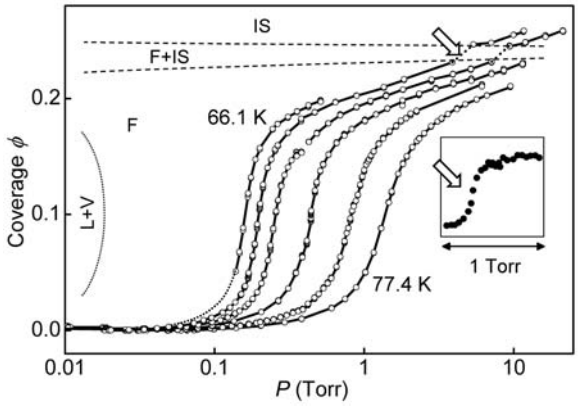

Fig. 2. Isotherms of coverage parameter φ for Ar on device YB3. The temperatures are 66.1, 67.7, 68.8, 71.0, 73.9, and 77.4 K. The large step occurs within the supercritical fluid (F), with a first-order L-V transition expected below a critical point at ~0.01 Torr. The smaller step, a separate measurement of which is shown in the inset, occurs at the transition to an IS. Dotted and dashed lines indicate boundaries of coexistence regions.

The fact that φ takes the value of 1/6 for the commensurate phase strongly indicates that the assumption behind Eq. 1 that $f_{res} \propto \rho^{-1/2}$ is justified for this device. Some other devices, including YB1 (Fig. 1E), showed similar responses but exhibited relatively small values of φ. This difference can be explained if these devices have a reduced ratio of available surface area to nanotube mass, which would be the case for a multiwalled nanotube or if part of the nanotube's surface were contaminated.

The identification of commensurate and incommensurate 2D solids on the cylindrical nanotube surface raises many interesting questions. The solid is subject both to the curvature, which breaks the isotropy of the graphene lattice, and to the cylindrical boundary condition. It may be rolled seamlessly like the underlying graphene, or alternatively it may contain a domain wall running along the nanotube. For the CS, which is in registry with the carbon surface, the seamless case occurs only when $(N - M)/3$ is an integer, where (N,M) is the nanotube's roll-up vector. Interestingly, this is precisely the same condition as for the nanotube to be metallic (*28*). From the V_g dependence of its conductance G (right inset to Fig. 3), we identify YB3 as a small-gap metallic nanotube that obeys this condition.

Because we can measure the electrical properties of the SWNT simultaneously with the mass absorption, we can quantitatively investigate the coupling between adsorbates and electrons. This is not possible in conventional adsorption experiments. Figure 4 shows the φ–P isotherm of Kr at 77 K for another device, YB8. It exhibits a large, sharp step at about 16 mTorr similar to that into YB3. (The smaller step pressure in YB8 can be explained by a larger binding energy due to a larger nanotube diameter.) The upper left inset shows G-V_g characteristics measured at pressures on either side of the phase transition. The conductance is suppressed at the higher pressure for positive V_g. The other trace in the main panel shows the resistance measured at a fixed positive gate voltage. It increases gradually at low coverages and jumps suddenly at the transition. This behavior is reproducible and reversible.

One immediate consequence of this observed coupling is that we can investigate the dynamics of such a phase transition. The right inset to Fig. 4 shows the resistance monitored with a 10-ms instrumental response time as the Kr pressure is increased rapidly across the transition. The step occurs in about 0.1 s, indicating that this is the intrinsic time scale of the phase transition on the SWNT.

Analysis of the G-V_g characteristics indicates that this SWNT has a small gap (~60 meV) and that the conductance is limited by tunneling across the gap at positive V_g but not at negative V_g (*20*). The larger decrease in conductance at the phase transition for positive V_g could thus be related to an increase in the gap. We note that the CS has a reciprocal lattice vector that connects the Dirac points in the graphene Brillouin zone, and hence coherent scattering from commensurate Kr offers a possible mechanism for modifying the gap. Also, the Kr atoms will be statically polarized by the gate-induced electric field perpendicular to the nanotube surface (*20*), thereby modifying their interactions with each other and with the substrate at high gate voltages. Further experiments of this type could yield many more important insights into the interaction of adsorbed substances with the electrons in graphitic carbon.

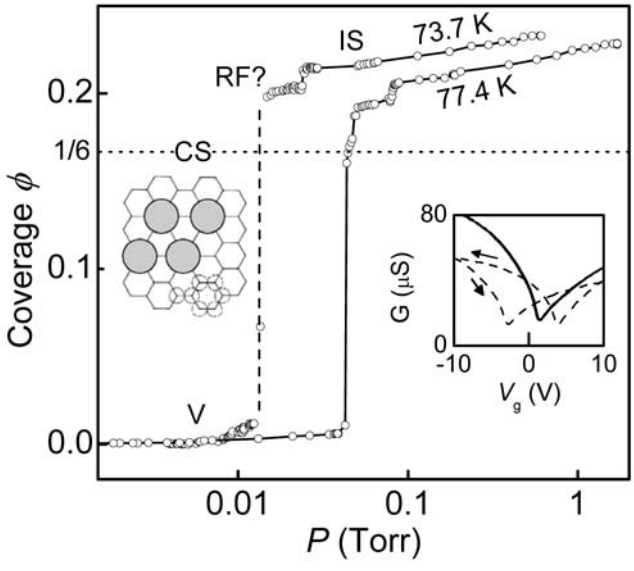

Fig. 3. Adsorption of Kr on device YB3, showing first-order phase transitions. (The 73.7 K isotherm has incomplete data at the dashed line.) The dotted horizontal line at φ = 1/6 corresponds to the expected coverage of 1 adsorbate per 6 carbon atoms in a commensurate solid on a clean SWNT. The left inset shows the commensurate arrangement of adsorbates (shaded circles) sitting on every third carbon hexagon. The right inset shows conductance versus gate voltage (solid: vacuum; dashed: in air, where there is hysteresis indicated by the arrows) at room temperature, whose form is that of a small-bandgap nanotube.

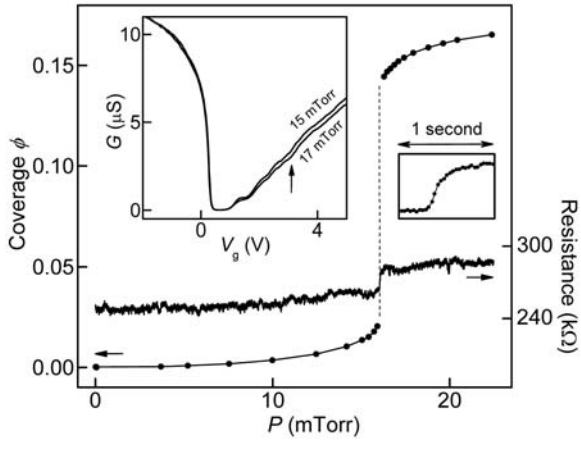

Fig. 4. Combined mass and transport measurements on device YB8 (1-μm gap) exposed to Kr at 77 K. Measurements are shown of both coverage parameter φ (left axis) and resistance R (right axis) as a function of pressure. The left inset shows conductance versus gate voltage at pressures just below (15 mTorr) and above (17 mTorr) the transition, with an arrow indicating the gate voltage of +3.1 V at which R was measured. The right inset shows resistance versus time during a rapid upward pressure sweep across the transition.

References and Notes

1. J. G. Dash, J. Ruvalds, *Phase Transitions in Surface Films*. Nato Advanced Study Institutes Series B (Plenum, New York, 1980), vol. 51.
2. L. W. Bruch, M. W. Cole, E. Zaremba, *Physical Adsorption: Forces and Phenomena*. (Oxford University Press, Oxford, 1997).
3. V. Sazonova *et al.*, *Nature* **431**, 284 (2004).
4. B. Witkamp, M. Poot, H. S. J. van der Zant, *Nano Lett.* **6**, 2904 (2006).
5. H. B. Peng, C. W. Chang, S. Aloni, T. D. Yuzvinsky, A. Zettl, *Phys. Rev. Lett.* **97**, 087203 (2006).
6. A. K. Hüttel *et al.*, *Nano Lett.* **9**, 2547 (2009).
7. J. Cao, Q. Wang, H. Dai, *Nat. Mater.* **4**, 745 (2005).
8. G. A. Steele, G. Gotz, L. P. Kouwenhoven, *Nat. Nanotechnol.* **4**, 363 (2009).
9. V. V. Deshpande *et al.*, *Science* **323**, 106 (2009).
10. G. A. Steele *et al.*, *Science* **325**, 1103 (2009).
11. B. Lassagne, Y. Tarakanov, J. Kinaret, D. Garcia-Sanchez, A. Bachtold, *Science* **325**, 1107 (2009).
12. R. Leturcq *et al.*, *Nat. Phys.* **5**, 327 (2009).
13. K. Jensen, K. Kim, A. Zettl, *Nat. Nanotechnol.* **3**, 533 (2008).
14. H. Y. Chiu, P. Hung, H. W. C. Postma, M. Bockrath, *Nano Lett.* **8**, 4342 (2008).
15. B. Lassagne, D. Garcia-Sanchez, A. Aguasca, A. Bachtold, *Nano Lett.* **8**, 3735 (2008).
16. W. Shi, J. K. Johnson, *Phys. Rev. Lett.* **91**, 015504 (2003).
17. M. R. Johnson *et al.*, *Chem. Phys.* **293**, 217 (2003).
18. J. C. Lasjaunias, K. Biljaković, J. L. Sauvajol, P. Monceau, *Phys. Rev. Lett.* **91**, 025901 (2003).
19. J. Cao, Q. Wang, D. W. Wang, H. J. Dai, *Small* **1**, 138 (2005).
20. Materials and methods are available as supporting material on *Science* Online.
21. A. D. Migone, Z. R. Li, M. H. W. Chan, *Phys. Rev. Lett.* **53**, 810 (1984).
22. F. Millot, *J. Phys. Lett.* **40**, 9 (1979).
23. G. Stan, M. W. Cole, *Surf. Sci.* **395**, 280 (1998).
24. A. Thomy, X. Duval, *J. Chim. Phys.* **66**, 1966 (1969).
25. M. D. Chinn, S. C. Fain, *Phys. Rev. Lett.* **39**, 146 (1977).
26. S. C. Fain, M. D. Chinn, R. D. Diehl, *Phys. Rev. B* **21**, 4170 (1980).
27. E. D. Specht *et al.*, *Z. Phys. B Condens. Matter* **69**, 347 (1987).
28. J. C. Charlier, X. Blase, S. Roche, *Rev. Mod. Phys.* **79**, 677 (2007).

29. We acknowledge useful discussions with M. Bockrath, H.-Y. Chiu, M. W. Cole, M. den Nijs, M. Schick, and A. van der Zande. This work was supported by grants from NSF

(DMR 0606078 and 0907690), the American Chemical Society Petroleum Research Fund, the University of Washington (UW) Royalty Research Fund, and a UW University Initiatives Fund fellowship. Portions of this work were done in the University of California at Santa Barbara Nanofabrication Facility and in the UW Nanotechnology Center, which are parts of the NSF-funded National Nanotechnology Infrastructure Network.

Supporting Online Material
www.sciencemag.org/cgi/content/full/327/5965/552/DC1
Materials and Methods
Figs. S1 to S3
References

28 September 2009; accepted 1 December 2009
10.1126/science.1182507

Spontaneous and X-ray–Triggered Crystallization at Long Range in Self-Assembling Filament Networks

Honggang Cui,[1] E. Thomas Pashuck,[1] Yuri S. Velichko,[1] Steven J. Weigand,[2] Andrew G. Cheetham,[3] Christina J. Newcomb,[1] Samuel I. Stupp[1,3,4,5]*

We report here crystallization at long range in networks of like-charge supramolecular peptide filaments mediated by repulsive forces. The crystallization is spontaneous beyond a given concentration of the molecules that form the filaments but can be triggered by x-rays at lower concentrations. The crystalline domains formed by x-ray irradiation, with interfilament separations of up to 320 angstroms, can be stable for hours after the beam is turned off, and ions that screen charges on the filaments suppress ordering. We hypothesize that the stability of crystalline domains emerges from a balance of repulsive tensions linked to native or x-ray–induced charges and the mechanical compressive entrapment of filaments within a network. Similar phenomena may occur naturally in the cytoskeleton of cells and, if induced externally in biological or artificial systems, lead to possible biomedical and lithographic functions.

One-dimensional (1D) objects in solution, such as carbon nanotubes (*1*), filamentous viruses (*2*), and rigid molecules (*3*), can spontaneously form orientationally ordered domains or networks as a result of their shape. This excluded volume effect is useful in the design of devices, liquid crystals, high-strength materials, bioactive hydrogels, and other functional structures. In biological systems, the bundling, orientation, and mechanical networking of 1D cytoskeleton components such as filamentous actin and microtubules mediate cellular events such as mitosis, protein transport, and signal transduction (*4*–*9*). Small-angle x-ray scattering (SAXS) can provide information on the size, shape, and symmetry of the internal domains of materials (*10*, *11*) and is extremely useful to study structures with the length scales of 3D networks formed by nanoscale filaments (*4*). However, x-ray beams can cause irreversible chemical changes that lead to detectable products at high fluxes and affect the formation of 3D structures (*12*–*14*). The typical mechanisms involve ejection of energetic electrons from molecules via the well-known photoelectric, Compton, and Auger effects and form free radicals and charged molecules, as well as chemical reactions (*15*–*19*).

We report the spontaneous and x-ray–triggered crystallization of supramolecular filaments within 3D networks at unexpectedly large distances (up to 320 Å). The filaments described here are formed by self-assembly in water of a synthetic molecule containing the short peptide sequence Ala_6Glu_3 (A_6E_3) covalently grafted to an alkyl chain of 16 carbons (fig. S1) (*20*). A representative cryogenic transmission electron microscopy (cryo-TEM) image is shown in Fig. 1A, revealing cylindrical nanofibers measuring ~102 Å in diameter corresponding to twice the fully extended length of the molecules. The length of the filaments cannot be directly obtained from cryo-TEM, but it is estimated to be on the scale of tens of micrometers. The combined effect of intermolecular hydrogen bonding among the peptide segments and hydrophobic collapse of hydrocarbon tails in these molecules leads to formation of the 1D nanostructures in dilute solution (*21*, *22*).

We observed that the SAXS profiles of 0.5 weight percent (wt %) solutions dramatically changed upon continuous x-ray exposure. Figure 1B displays 50 sequential SAXS profiles of the same spot with an exposure time of 4 s each, plotted on a double-logarithmic scale. The first spectrum (red) shows a typical scattering profile of cylindrical objects in solution, as suggested by the –1 slope in the low q region and a diffuse form factor peak around 0.1 $Å^{-1}$ (fig. S2) (*20*, *23*). Successive irradiation on the same spot yielded a series of Bragg peaks. The relative positions of the peaks follow the q/q^* ratios of $1 : \sqrt{3} : \sqrt{4} : \sqrt{7} : \sqrt{9} : \sqrt{12}$ (where q^* is the principal peak position), characteristic of a highly ordered 2D hexagonal lattice (space group *p6mm*). The development of scattering profiles is characterized by the emergence and continued increase in intensity of the principal Bragg peak, as well as the appearance of additional peaks at higher q values. Figure 1C shows the 2D scattering patterns of the first and the last exposures, revealing the disorder-to-order transition. The low volume fraction of filaments (0.5 wt %) indicates that these hexagonally packed 1D objects must exist as bundles. We measured the final values of full width at half maximum and used the Scherrer equation to estimate a bundle size. The calculation yields a value of about 1 μm; however, given the size regime the absolute value obtained from the Scherrer equation is of questionable accuracy. The Debye-Sherrer ring–like pattern after x-ray exposure is typical of scattering from a powder sample, implying that these hexagonal crystalline bundles are randomly distributed in solution (Fig. 1D).

We found that this x-ray–triggered structural rearrangement only occurred at relatively low concentrations. Figure 2A shows a similar disorder-to-order transition observed at 1 wt % upon continued x-ray irradiation. However, at higher concentrations (2 wt % and higher), the Bragg peaks could be observed without the need for continuous x-ray irradiation (Fig. 2, B and C). The hexagonally stacked filaments at 2 wt % and 5 wt % were stable during x-ray exposure, and their corresponding Bragg peak positions did not shift by more than 3% with accumulated exposure time.

These observations suggest that hexagonal stacking of filaments at higher concentration is a spontaneous process and not associated with x-ray irradiation. We plot the x-ray profiles corresponding to the last exposure for various concentrations in Fig. 2D. Five to seven Bragg peaks are registered in each scattering profile and have the expected relative ratios of hexagonal structures. The Bragg peak positions shift smoothly to higher values of q with an increase in peptide concentration in both spontaneous and x-ray–triggered hexagonal structures. These changes correspond to a decrease in interfilament separation as the concentration rises (Fig. 2E) and suggests the spontaneous and x-ray–triggered hexagonal structures emerge through similar mechanisms.

To determine whether x-ray beam heating could contribute to this structural disorder-to-order

[1]Department of Materials Science and Engineering, Northwestern University, 2220 Campus Drive, Evanston, IL 60208, USA. [2]DuPont-Northwestern-Dow Collaborative Access Team (DND-CAT) Synchrotron Research Center, Northwestern University, Advanced Photon Source (APS)/Argonne National Laboratory 432-A004, 9700 South Cass Avenue, Argonne, IL 60439, USA. [3]Institute for BioNanotechnology in Medicine, Northwestern University, Chicago, IL 60611, USA. [4]Department of Chemistry, Northwestern University, 2220 Campus Drive, Evanston, IL 60208, USA. [5]Department of Medicine, Northwestern University, 2220 Campus Drive, Evanston, IL 60208, USA.

*To whom correspondence should be addressed. E-mail: s-stupp@northwestern.edu